

Systematics and efficiencies for the multiplicity
dependent D^{*+} meson measurement in 7 TeV
proton-proton collisions at ALICE

Guanqiao Li
Studentnumber: 3535452
Utrecht University

June 14, 2013

Abstract

This thesis focuses on the extraction of the raw yield of reconstructed D^{*+} mesons and its systematics and efficiency in different p_T and multiplicity intervals in proton-proton collisions at $\sqrt{s} = 7$ TeV. The yield is extracted from data samples required from the ALICE detector measured in 2010 over four time periods with topological selection and 3σ particle identification (PID) cuts. The purpose of this work is to analyze the open charm production dependence on the multiplicity. It is expected that the production probability would increase with multiplicity due to the increase in the hardness of the collision. However, if multi-parton interactions play a large role at LHC we can expect the increase to be much more steep than what is expected from theoretical models based on single-parton interactions. The final result of the D^{*+} vs multiplicity analysis is expected to increase the knowledge of the multi-parton interaction phenomena.

Contents

1	Introduction	2
1.1	Multi-parton interactions	3
1.2	Motivation	3
2	The ALICE detector	5
2.1	Inner Tracking System	6
2.2	Time Projection Chamber	7
2.3	Time Of Flight	7
3	Data samples	10
3.1	Systematics on the multiplicity determination	11
4	D*+ mesons	15
4.1	Open charm production	15
4.2	D*+ reconstruction	16
4.3	Selection cuts	17
5	Yield extraction	22
6	Systematics	24
6.1	Systematics on the yield extraction	24
6.1.1	Different invariant mass ranges	25
6.1.2	Different background function	25
6.1.3	Bin counting	25
6.2	Results	26
7	Efficiency corrections	30
7.1	Monte Carlo simulations	30
7.2	Efficiency	31
8	Conclusions	33
8.1	Further research	33
A	Discussions	35
A.1	Sigmas	35
A.2	Ratios	36

Chapter 1

Introduction

The theory for strong interactions is called Quantum Chromodynamics (QCD). It describes the interactions between colored objects which are quarks and gluons, also known as partons. Quarks can carry three types of color (red, green and blue) while gluons which are the force carriers in QCD, carry combinations of a color and anti-color which does not necessarily have to be color neutral, this is why the gluons can self-interact. The strength of the strong interaction is described by the coupling constant α_s . For the estimation of α_s at asymptotically large momentum transfer Q the coupling constant vanishes [1], this is known as the asymptotic freedom. In contrast to the low momentum transfer, the coupling constant only increases. This means that when a quark pair try to separate, the gluon field between the quarks like a color flux tube connecting the quarks. Figure 1.1 shows a schematic representation of the gluon field between two quarks at different separation distances.

Because gluons can self-interact, these gluons can form a new quark anti-quark pair when enough energy is available in the flux tube, this process is called string-fragmentation [2]. This explains why in nature quarks are always bounded in groups having a neutral net color (white). This group of quarks and gluons is called hadrons.

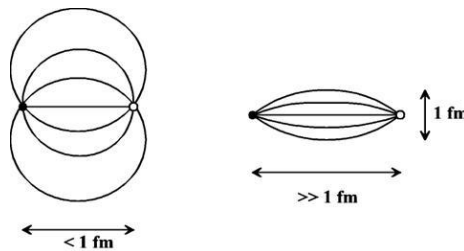


Figure 1.1: A schematic representation of the gluon field between two quarks. At small distances the $1/r$ term in the potential energy dominates so the field has a Coulomb like structure and at large distances the linear (r) term dominates so the field confines itself to a more tubelike structure.

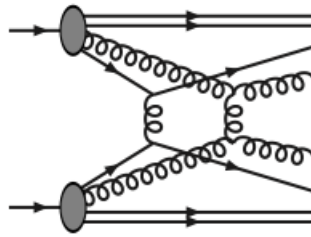


Figure 1.2: A schematic sketch of a pp collision with $2 \rightarrow 2$ perturbative interaction. The circles represent the partons, the straight lines represent the constituent quarks and the curled lines represent gluons [3].

1.1 Multi-parton interactions

Due to the composite nature of the hadron, it is possible that in a collision (event) of two hadrons at high energy multiple partons can collide during a single hadron collision. This is called multi-parton interaction. Figure 1.2 shows a Feynman diagram of a single parton-parton collision in a proton-proton (pp) collision.

In the case of single parton interactions, one can expect that the charm production probability would increase with the charged particle multiplicity. This is due to the increase of hardness of the collision. The hardness is determined by the centrality of the collision. The centrality is theoretically characterized by the impact parameter \mathbf{b} , where \mathbf{b} is the distance of closest approach. If the collision is head-on, low centrality, then partons collide with more energy resulting in a higher particle production, this process is hard. At high centrality, peripheral collision, the collision have less energy resulting in a lower particle production. This process is soft.

If the multi-parton interactions would play a significant role, then a steeper increase in the charm production probability would be expected at higher charged particle multiplicity. Such behavior is expected to deviate significantly from the predictions of single parton interaction at higher multiplicity.

For single parton interactions the cross section $\sigma_{parton-parton}$ lies between 0 and 1. But for multi-parton interactions it is also possible that the integrated cross section σ_{int} can exceed 1, this indicates that σ_{int} can exceed the total inelastic, non-diffractive cross section σ_{tot} . The parton interactions can be described by a Poisson distribution, assuming that per event the parton interactions take place independently from each other. The number of parton interactions can be estimated by:

$$N_{parton-parton} = \frac{\sigma_{int}}{\sigma_{tot}} [4][5]. \quad (1.1)$$

1.2 Motivation

Now that we know that hadrons can be described by groups of elementary constituents called partons, we can conclude that the multi-parton interaction is a direct consequence of the nature of the hadron and that the phenomenon must always exist at some level in the hadron collision. It can cause non-trivial changes to the color topology of the colliding systems as a whole which has po-

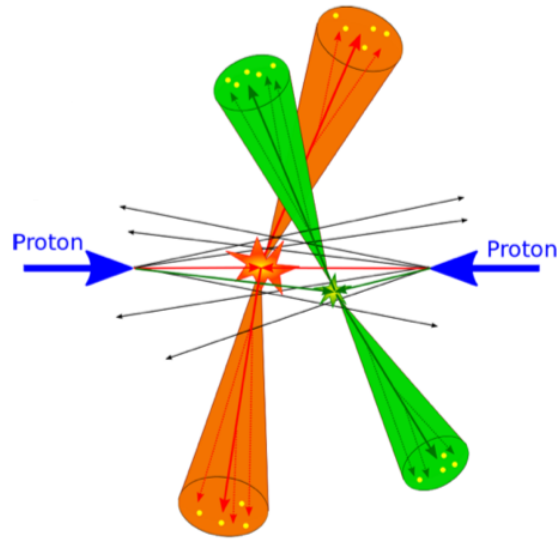


Figure 1.3: A schematic representation of a double parton interaction with pair-wise p_T -balanced jets in a single pp collision [6].

tentially drastic consequences for the particle multiplicity (multiplicity in short) in the final state [3].

The present energies generated by the LHC are so high that the de Broglie wavelengths of the partons are now much smaller than the size of the hadron. This results into the partons behaving more like a particle, making the contribution of the multi-parton interaction increasingly important for future measurements. Observables like the multi-jet, transverse momentum spectra, the underlying event and the charged particle multiplicity that depend on the multi-parton interaction number, indicate that the multi-parton interaction may represent a significant background to discovery channels [4]. Multi-parton interaction dependent observables, like multi-jets indicate a higher production of particles. Figure 1.3 shows a sketch of two parton interactions in a single pp collision.

This thesis will focus specifically on the reconstruction of the D^{*+} meson. The reason why the D^{*+} was chosen, is because it contains a charm quark and it gives a clean signal in pp collisions. Moreover it is the heaviest charmed mesons produced at a reasonably high rate having a mass of $2010.28 \pm 0.13 \text{ MeV}/c^2$ [7]. Since the mass of the D^{*+} is only a few hundreds of MeV larger than the mass of the D^0 (one of its daughter particles), the mass difference is $145.421 \pm 0.010 \text{ MeV}/c^2$. One should expect a clear peak with respect to the uncorrelated background in the invariant mass difference (ΔM) distribution. Chapter 4 will discuss the decays of the D^{*+} meson. By determining the number of D^{*+} meson produced, we know the number of prompt charm quarks produced in a pp collision, thus by comparing the results with theory one can determine how much the multi-parton interactions will influence the particle production dependent on the multiplicity.

Chapter 2

The ALICE detector

ALICE is one of the four main detectors at the LHC. It was designed to measure the particles produced in the collisions in the most complete way possible, so that we can study and reconstruct the evolution of the system in time and space. Figure 2.1 shows the schematic representation of the ALICE detector. Before we discuss the detectors a few variables need to be introduced. The pseudorapidity η defined as:

$$\eta = \frac{1}{2} \log \frac{|\mathbf{p}| + p_z}{|\mathbf{p}| - p_z}. \quad (2.1)$$

Here η is given as the angle with respect to the beam axis (z-axis), where $\eta = 0$ corresponds to the perpendicular direction to the beam axis, and $\eta = \infty$ corresponds to the parallel direction to the beam axis.

Another variable, related to the pseudorapidity is the rapidity y defined as:

$$y = \frac{1}{2} \log \frac{E + p_z}{E - p_z}. \quad (2.2)$$

The ALICE detector consist of a vacuum pipe for the beam to travel through and around it are numerous subdetectors each fulfilling a function of detecting particles flying of a collision and a solenoidal magnet in the central part which can reach up to 0.5 T.

For extracting information about the collision, one can measure the remnants of the colliding nuclei with the ZDC (Zero Degree Calorimeter, placed about 110 meters from the primary vertex). With the FMD (Forward Multiplicity Detector, with a coverage of $1.7 < |\eta| < 5.1$), V0 and T0 one can measure the number of particles produced in the collision and their spatial distribution. The V0 is also used to register the start of the events. When certain conditions are met during the detection of events it can trigger the other subdetectors to start with their processes, the T0 and the Time Of Flight (TOF) (explained in 2.3) register the travel time of a particle to travel from the T0 to the TOF.

For tracking particles to precisely know the trajectory, we use the ITS (Inner Tracking System, explained in 2.1).

One of the purposes of the ITS, TPC (Time Projection Chamber, explained in 2.2) TOF and the muon spectrometer is the particle identification.

The ITS, TPC and TOF are the most important detectors during the analysis, so these will be explained in more detail.

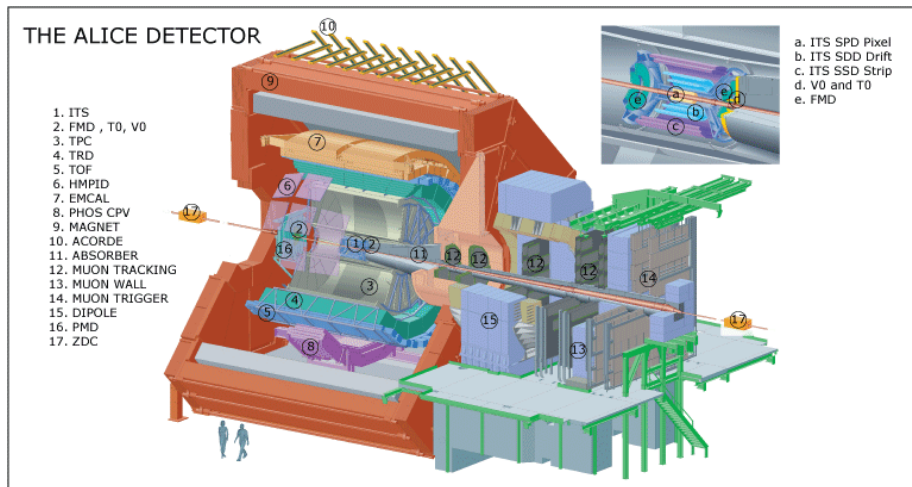


Figure 2.1: Layout of the ALICE detector.

2.1 Inner Tracking System

The ITS is the detector that lies the closest to the barrel where the beam passes. It contains a total of six cylindrical silicon layers wrapped around the beam pipe covering a central rapidity of $|\eta| \leq 1$ [8], the layers are categorized in groups of 2 layers. The first group of layers is called the SPD (Silicon Pixel Detectors), the second group is the SDD (Silicon Drift Detectors) and the last group is the SSD (Silicon Strip Detectors). Figure 2.2 shows a schematic representation of the ITS with the three detectors. For the first layer the distance to the interaction point is 3.9 cm and for the second layer 7.6 cm. For the SDD it is for the first 15 cm and 23.9 cm for the second. And for the SSD it is 38 cm for the first and 43 cm for the second.

The ITS is used to localize the primary vertex and reconstruct the secondary vertices, track and identify low momentum particles (≥ 100 MeV/c), improve momentum and angle resolution of high p_T particles and reconstruct particles traversing dead regions of the TPC. For this analysis we use it to reconstruct the secondary vertex which will be the location where the D^0 decays into a K^- and a π^+ .

Because the SPD is located so close to the interaction point, it will then operate in a high track density region where the density can reach up to 80 tracks/cm². To cope with such high densities, high precision and granularity are mandatory. Therefore the first two layers are made out of silicon pixels, because they have the largest spatial precision in $r\phi$ compared with the SDD and SSD. Table 2.1 shows the spatial precision values of the three detectors. The SDD measures the drift time of an energetic charged particle traversing the detector, so that it can reconstruct the radial distance of the traversal point of the particle [9]. The SSD is used to connect the ITS tracks to the TPC tracks and provide dE/dx information to assist particle identification for low momentum particles.

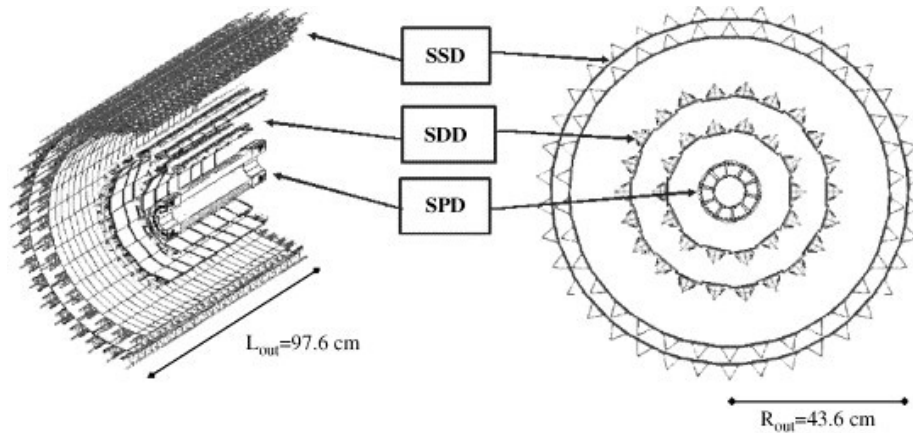


Figure 2.2: Layout of the ITS.

parameter	Silicon Pixel	Silicon Drift	Silicon Strip
$r\phi$ (μm)	12	38	20
z (μm)	100	28	830

Table 2.1: Spatial precision parameters of various detector types. A module represents a single sensor element [8].

2.2 Time Projection Chamber

The main tracking detector in the central barrel of the ALICE detector is the TPC detector. The layout of the TPC is shown in figure 2.3. The TPC is basically a giant gas chamber containing originally 90% Ne and 10% CO₂, but more recently it was proposed to add 5% N₂ to the mixture, which would provide higher gas gain stability and a better control of the fraction on N₂ and its influence of the drift velocity [10]. When a charged particle passes through the gas it ionizes the gas, that way the path of the particle can be tracked with an efficiency of <90%. Other functions are measuring the momentum of charged particles, particle identification by dE/dx measurements and two-track separation in the region of $p_T < 10$ GeV/c and $|\eta| < 1$.

To identify the type of the particle one can look at the energy loss of the particles. Figure 2.4 shows such a measurement. The figure shows that the particle species line up in bands according to their mass and charge and as dE/dx and p_T are both determined from the TPC there is no possibility for mismatches at low momentum. By parametrizing these distributions, for example for the kaon, one can say with a certain probability σ , that the particle has a probability of 68% to be a kaon. The procedure described here is called PID (particle identification).

2.3 Time Of Flight

Behind the TPC is the TOF detector, which measures the time needed for a particle to travel from T0 to TOF. When a particle passes the T0, it triggers the

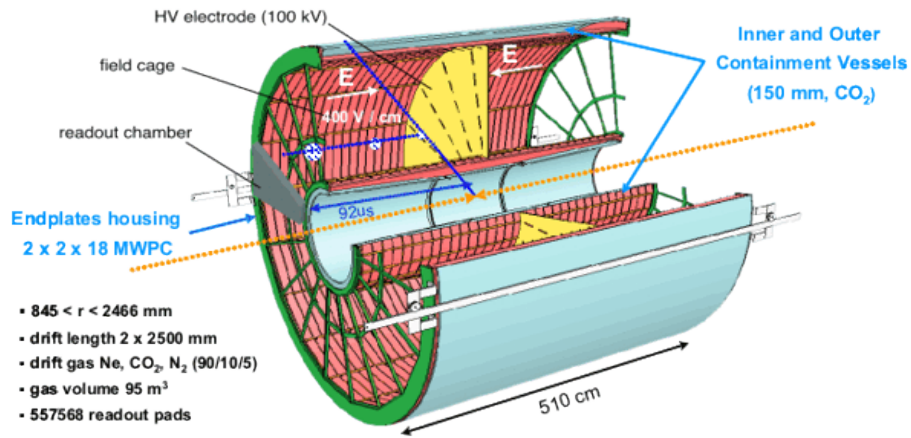


Figure 2.3: Layout of the TPC detector.

TOF to start timing. This is because heavier particles have a lower speed than lighter particles, so there must be significant differences in travel time between heavy and light particles. The TOF and T0 have a combined resolution of 150 ps (TOF has alone 100 ps).

By measuring the time, one can identify the particle specie by using the same method for parametrizing the distribution given in figure 2.5 as in the dE/dx distribution.

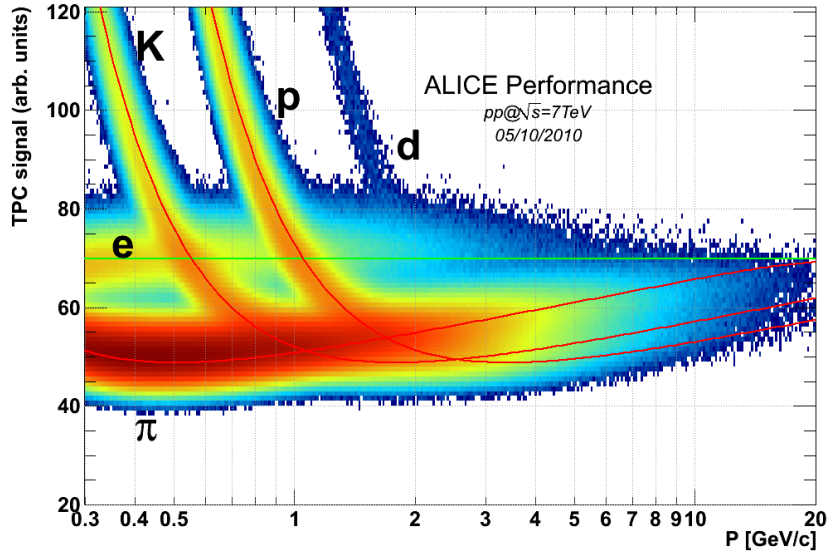


Figure 2.4: TPC signal as function of momentum for particles produced in pp collisions at $\sqrt{s} = 7$ TeV [11].

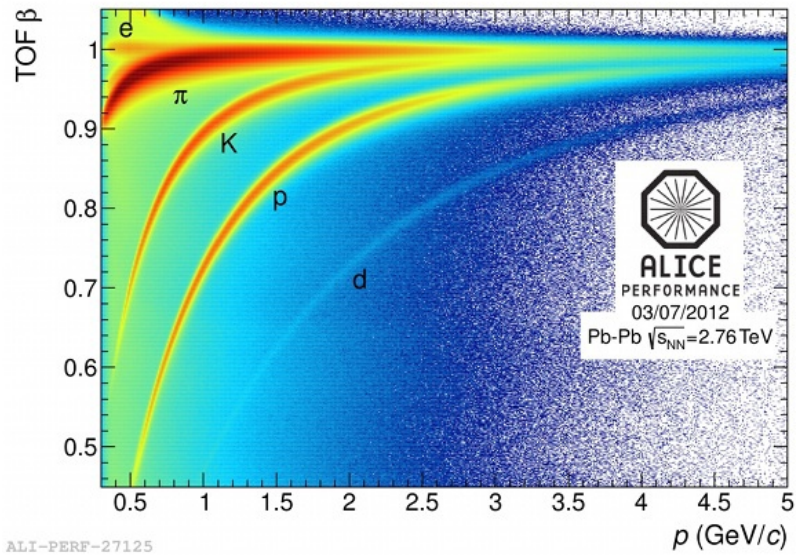


Figure 2.5: Particle velocity $\beta = v/c$ as measured with the ALICE TOF detector as a function of the particle momentum p for a data sample taken with heavy-ion collisions provided by the LHC in the year 2011 [12].

Chapter 3

Data samples

This thesis uses the data samples measured by the ALICE detector in 2010 from the periods: b, c, d and e. We also use data samples where a high multiplicity trigger is used. These are data samples from pp collisions at $\sqrt{s} = 7$ TeV. Table 3.2 shows the number of events in each period. Please note that the amount of event in the data samples used in this thesis is only a fraction ($\sim 2/3$) of the total amount of event measured in the four periods, thus it does not contain the full statistics.

The particle multiplicity is measured using the SPD (we use the two layers of SPD to prevent tracks caused by interaction with the detector as much as possible). When a particle passes a pixel, it will give a hit on the detector. By constructing every possible line between a hit from the first layer and the second, then by subtracting the tracks for which it is impossible to originate from our primary vertex, we then remain with an amount of track originating from the primary vertex, this amount will be proportional to the multiplicity in the region of $|\eta| \leq 1$.

Because the interval of each period in which the data samples were taken are in the order of months, we must take into account that there are influences beyond our control like change of seasons (temperature differences, humidity, etc.) or aging problems (decrease of acceptance) of the detector. This is done by taking one set of measurements and then to normalize the data of the other periods with a normalization factor:

$$N_{corr} = \frac{\langle N_{tracklets}^{ref} \rangle}{\langle N_{tracklets}^i \rangle} N_{raw}, \text{ where } i = c, d, e. \quad (3.1)$$

Here $\langle N_{tracklets}^{ref} \rangle$ is the highest mean number of tracklets in the reference z-vertex bin in period b with a value of 9.26 and $\langle N_{tracklets}^i \rangle$ is the mean number of tracklets for events with vertex at given value z (with z inside the range $|z| < 10cm$) for the period that will be normalized. z or z_{vtx} is the position of the primary vertex in the z-axis. N_{raw} is the number of events in the uncorrected tracklet distribution and N_{corr} is the number of events for the corrected tracklet distribution. Figure 3.1 shows the plot of the tracklet profiles of all four periods versus the z-vertex. All other periods are normalized to period b, the reason we took period b is because we assume that the detector does not suffer from aging problems at the beginning of the experiment, thus having the highest

acceptance of the four periods. From table 3.2 we can see that the normalized mean of the four period are almost the same.

Table 3.2 also show that the total amount of events in each period is very different, this is also why we need to scale the distributions of period c, d and e to scale to period b. This is done by adding a factor N_b/N_i , ($i = c, d, e$) to the distributions of period c, d and e, where N_b is the total number of events in period b and N_i is the total number of events of the period that will be scaled. Figure 3.2 shows the distribution of the four periods uncorrected and corrected with the normalization factors.

3.1 Systematics on the multiplicity determination

We have just discussed that during the measurements in different periods, the tracklets distribution can vary. Figure 3.2(b) shows that at low multiplicity the distributions overlap each other, but when the multiplicity increases the distributions start to deviate. It is then important to know how much this deviation is, because we are analyzing the number of D^{*+} mesons in different multiplicity intervals by summing the events of all the periods in a certain multiplicity interval. By analyzing the difference of the distribution of the different periods we can get a systematic uncertainty of the detector in the different periods. This can be added to the systematic uncertainties in table 6.2.

Figure 3.3 shows the ratios of the different periods. At low multiplicity the ratios are all at 1, but at a multiplicity of 50 some ratios are clearly deviated from 1. The ratios of c/b, d/c and e/d are $\leq 10\%$, each of these period pairs lie chronologically next to each other, the explanation for this pattern is that the time between each of these two periods are at a minimum so the condition differences during the measurement are also very small. Table 3.1 shows the spread of the ratios between the different periods.

Ratio	Spread (%)
c/b	~ 7
d/b	~ 15
e/b	~ 20
d/c	~ 7
e/d	~ 4
e/c	~ 14

Table 3.1: The spread of the ratio of the four periods.

Period	Events ($\times 10^6$)	Mean uncorrected	Mean corrected
b	5.4	~ 8.76	~ 9.25
c	53.1	~ 8.07	~ 9.26
d	107.0	~ 7.48	~ 9.26
e	75.0	~ 7.31	~ 9.26

Table 3.2: The number of events per period. The uncorrected mean is the expected value of the uncorrected tracklets distribution and the corrected mean is the expected value of the normalized (corrected) tracklets distribution. The number of events shown in b is a fraction of the total number of events measured in that period, so the uncorrected mean is the mean of just a fraction of the total number of events and the corrected is the mean of the total number.

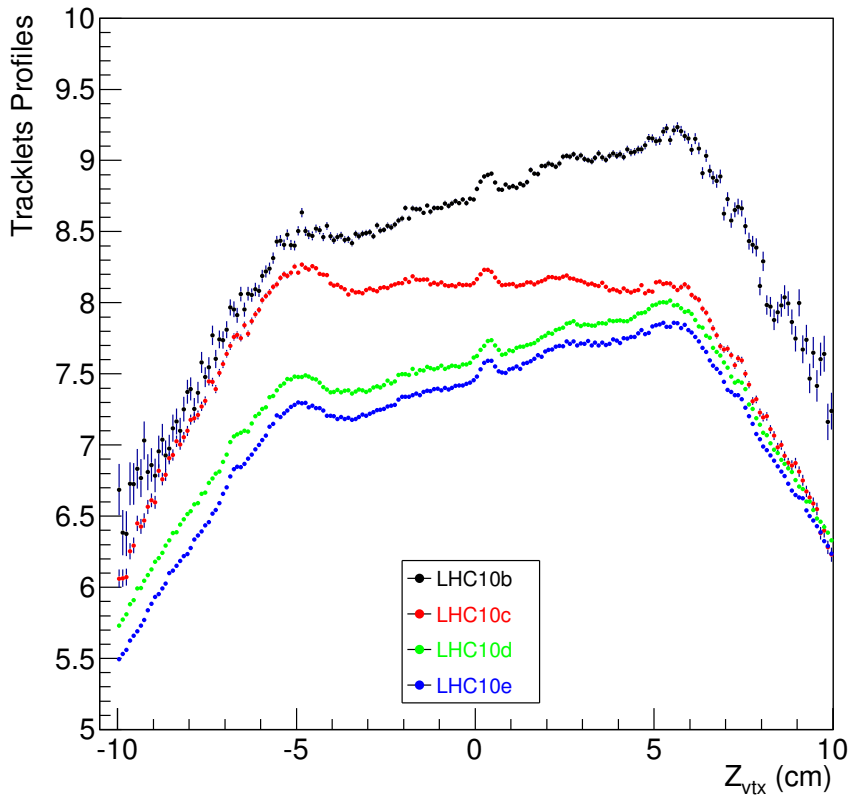
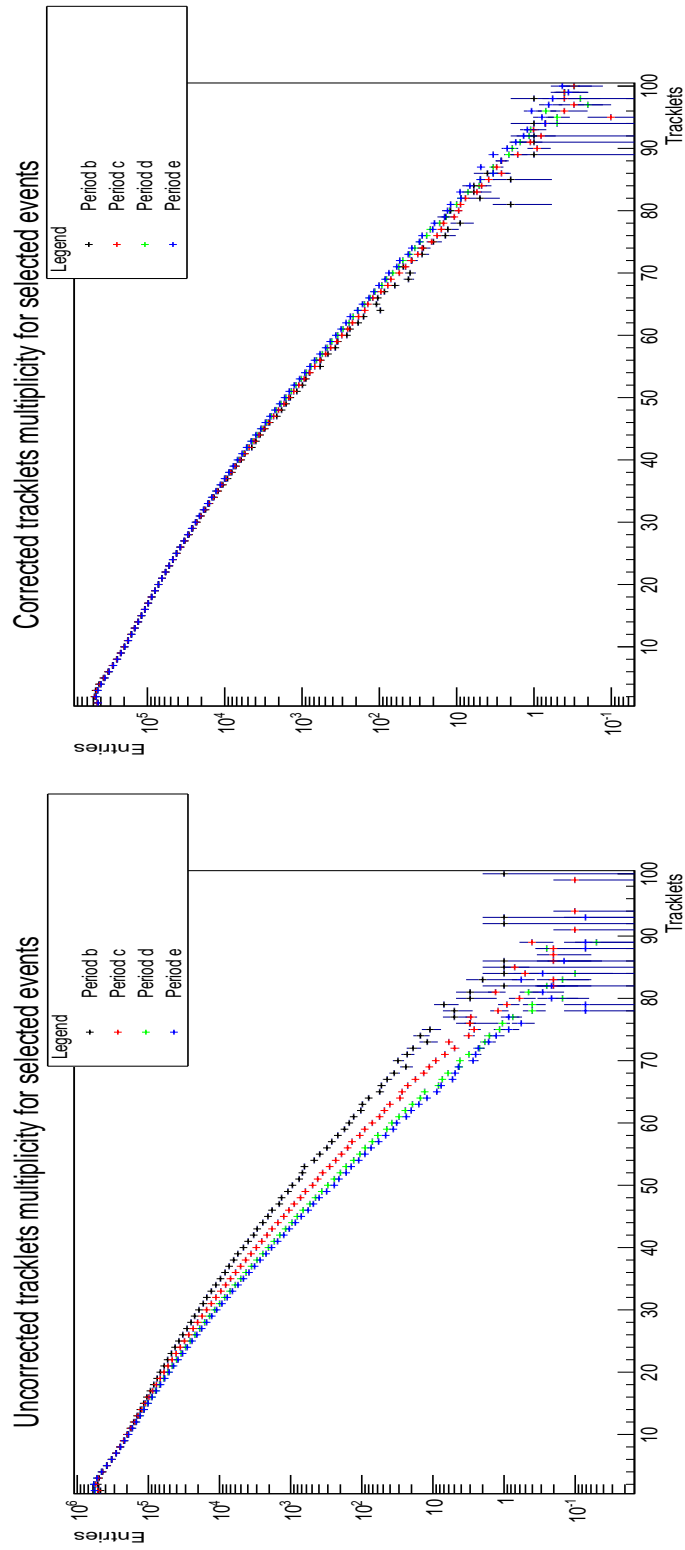


Figure 3.1: The uncorrected profiles ($\langle N_{tracklets} \rangle$) of all four data sets versus the z -vertex.



(a) (b)
 Figure 3.2: (a) Is the uncorrected distribution of events versus tracklets and (b) is the corrected distribution. The y-axis on both are at logarithmic scale.

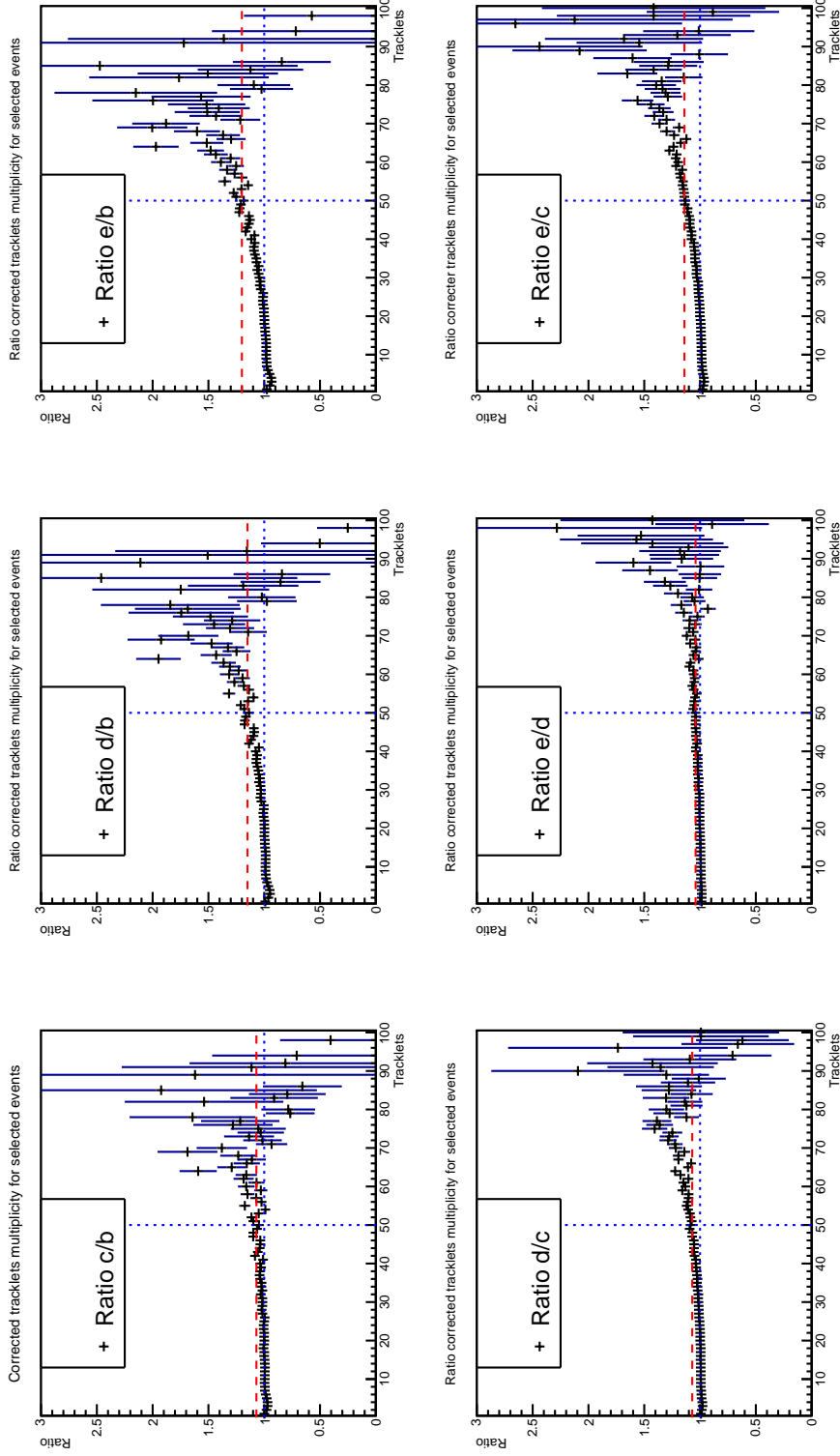


Figure 3.3: The ratio of the multiplicity distributions of the periods b, c, d and e. The horizontal blue dashed line is the indication of ratio = 1, the vertical blue dashed line is to indicate that the spread of the ratio is taken at a multiplicity of 50 and the red line is the spread of the ratio.

Chapter 4

D^{*+} mesons

This chapter begins with an introduction to the D^{*+} and D⁰ meson, its reconstruction and its decay modes. Then we will go on to the selection of D^{*+} candidates, and then to the extraction of the yield (the integral of the gaussian within the 3 σ width).

The D^{*+} meson ($2010.28 \pm 0.13 \text{ MeV}/c^2$ [7]) consists of a charm quark (c) and an anti-down quark (\bar{d}). In this analysis we consider two types of mechanisms through which a charm quark can be created during a high energy collision, these are: Pair production and gluon splitting. In pair production a pair of partons will interact with each other forming a pair of quarks (q \bar{q}), in gluon splitting two gluons will interact, producing two gluons again, but now one gluon will split into a q \bar{q} pair.

A D^{*+} is unstable, it cannot reach the detector thus it can never be observed directly. The D^{*+} has a total of three decay modes, but for this analysis we will only look at the one with the highest branching ratio: D^{*+} \rightarrow D⁰ π_s^+ ($\Gamma_i/\Gamma = 67.7 \pm 0.5\%$). π_s^+ is a soft pion, it only has a momentum of 39 MeV/c [13] in the rest frame of the D^{*+}. As a consequence the signal seen in the $\Delta M = M_{D^{*+}} - M_{D^0}$ is close to the mass of the pion ($139.57018 \pm 0.00035 \text{ MeV}/c^2$). The D⁰ ($m = 1864.86 \pm 0.13 \text{ MeV}/c^2$) also decays before it reaches the detector, here we are interested in the decay mode: D⁰ \rightarrow K⁻ π^+ ($\Gamma_i/\Gamma = 3.89 \pm 0.05\%$).

4.1 Open charm production

The production of the charm quark can be predicted by pQCD, because its mass is $1.275 \pm 0.025 \text{ GeV}/c^2$. Its mass is then larger than the QCD scale parameter $m_Q > \Lambda_{\text{QCD}}$, which assures the reliability of the calculations of pQCD. Our current theoretical models are still incomplete, this is because non-perturbative phenomena have important contributions to the heavy flavor production. The calculations currently available are performed by matching the resummation of logarithms of the transverse momentum over the mass of the quark at next-to-leading-logarithm (NLL) accuracy. For massive quarks one uses calculations at the first-order-next-to-leading-logarithm (FONLL) [14].

Figure 4.1 displays the three mechanisms for quark production, the pair creation

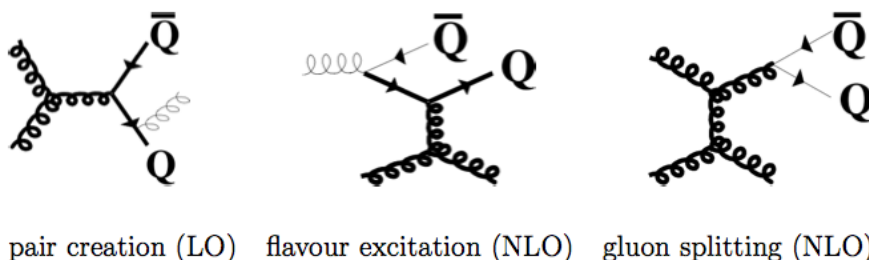


Figure 4.1: The Feynman diagrams of the three possible mechanisms for quark production. The thick lines represent hard processes, the thin lines correspond to the initial or final state parton shower. The straight lines are quarks and the curled lines gluons.

at leading-order level ($q\bar{q} \rightarrow Q\bar{Q}$ and $g\bar{g} \rightarrow Q\bar{Q}$), the flavor excitation at next-to-leading-order level ($qQ \rightarrow qQ$ and $gQ \rightarrow gQ$) and the gluon splitting at next-to-leading-order level ($g \rightarrow Q\bar{Q}$). In this thesis we will only look at the gluon splitting and pair creation processes.

4.2 D^{*+} reconstruction

To reconstruct the D^{*+} meson we first need to reconstruct the D^0 . The D^0 is a very unstable, it will decay before it reached the detector so we cannot detect it directly, thus we must focus on its daughter particles K^- and π^+ . We start with combining the negative and positive tracks belonging to a single event using a reconstruction algorithm, thus giving us the total amount of tracks of K^- and π^+ particles. Note that these tracks do not all come from the D^0 decay, the ones not coming from the decay produce the background in the invariant mass distribution. By applying selection cuts we can reduce the background with respect to the signal. The invariant mass is thus given by:

$$M(K\pi) = \sqrt{(E_K + E_\pi)^2 - (\mathbf{p}_K + \mathbf{p}_\pi)^2}, \quad (4.1)$$

\mathbf{p}_K is the momentum vector of the kaon and \mathbf{p}_π is that of the pion and E_K and E_π their respective energies:

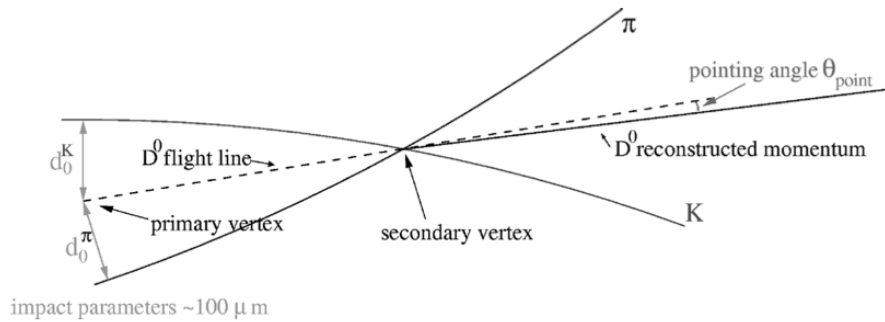
$$E = \sqrt{m^2 + \mathbf{p}^2}. \quad (4.2)$$

Equation 4.2 is a general expression for the energy of a particle. The particles that come from the actual secondary vertex will have an invariant mass that lies within a certain range, depending on the accuracy of the detector, of the mass of the D^0 . We only select candidates that have an invariant mass within this range, this is known as the D^0 mass window.

Now if we want to reconstruct the D^{*+} we have to combine the tracks of the D^0 with the soft pion. This gives an invariant mass of:

$$M(K\pi\pi) = \sqrt{(E_K + E_\pi + E_{\pi_s})^2 - (\mathbf{p}_K + \mathbf{p}_\pi + \mathbf{p}_{\pi_s})^2}. \quad (4.3)$$

Here we can select candidates that have an invariant mass of $M(K\pi\pi)$, this is called a peak-window.

Figure 4.2: D^0 decay with different parameters [14].

Now having both the invariant masses of D^0 and D^{*+} , we can take the mass difference of the two.

$$\Delta M = M(K\pi\pi) - M(k\pi). \quad (4.4)$$

Doing this results into a very clear peak making it easier to detect, even if the background would become large.

4.3 Selection cuts

Now that we have a reconstruction of the D^{*+} and D^0 we want to reduce the background. To reduce the combinatorial background we can apply cuts on the topology of the D^{*+} and D^0 decay. Figure 4.2 shows a sketch of the D^0 decay where the primary vertex is the collision point, the secondary vertex the D^0 decay point, d_0^K and d_0^π the impact parameters of the kaon and pion and the pointing angle Θ_{point} . The flight line is constructed from the two vertexes and with the tracks of π and K the momentum of the D^0 can be constructed. This gives us the pointing angle, the angle between the flight line and reconstructed D^0 momentum. By extrapolating the tracks of the pion and kaon backwards, we can define the impact parameter as the distance of closest approach between the tracks and the primary vertex, d_0^K and d_0^π .

PID cuts are also done using the TOF and TPC detectors. Figure 4.4 shows two invariant mass distributions of ΔM in the same p_T interval and same multiplicity interval, but one includes the whole background and at the other a PID cut has been used. In this analysis a PID cut of 3σ on both TOF and TPC is used. This means that the dE/dx of kaon and pion shown in figure 2.4 and the velocity β in figure 2.5 are standard distributions with the mean at the theoretical function line given by the red lines. Then we take the region of a width of 3σ . When an ΔM distribution is fitted, we look to optimize the significance. The significance is defined as:

$$\mathcal{S} = \frac{S}{\sqrt{S+B}}, \quad (4.5)$$

\mathcal{S} is the statistical significance, S is the number of entries in the signal range and B is the number of entries of the background in the signal range. The significance gives the probability of the peak being a result of the D^{*+} or background fluctuation. The norm is that for $\mathcal{S} \geq 3\sigma$ we may conclude that we found a signal and for $\mathcal{S} \geq 5\sigma$ we may conclude we found a particle. The set of D^{*+}

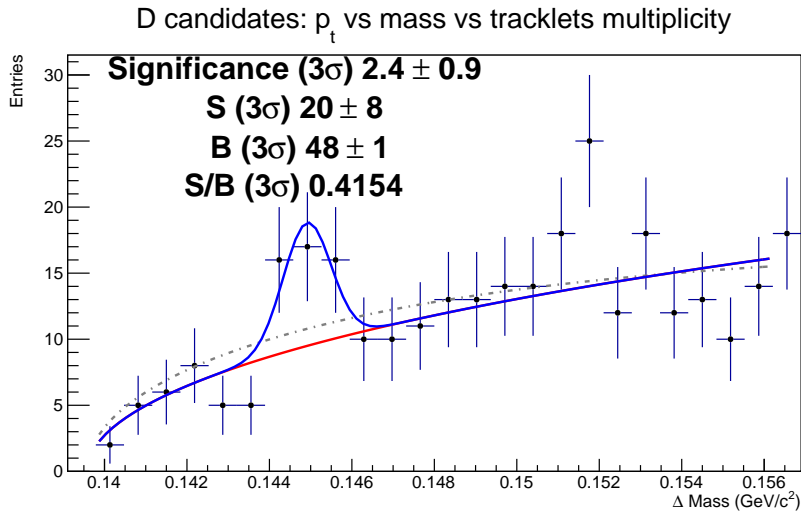
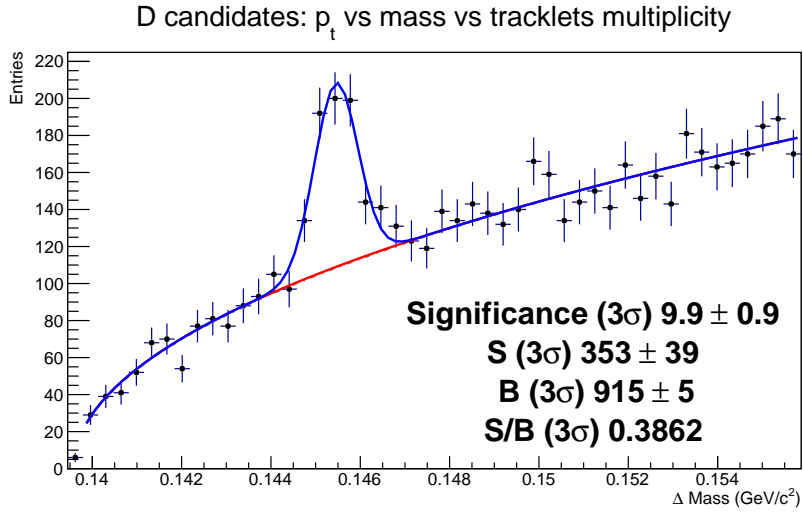


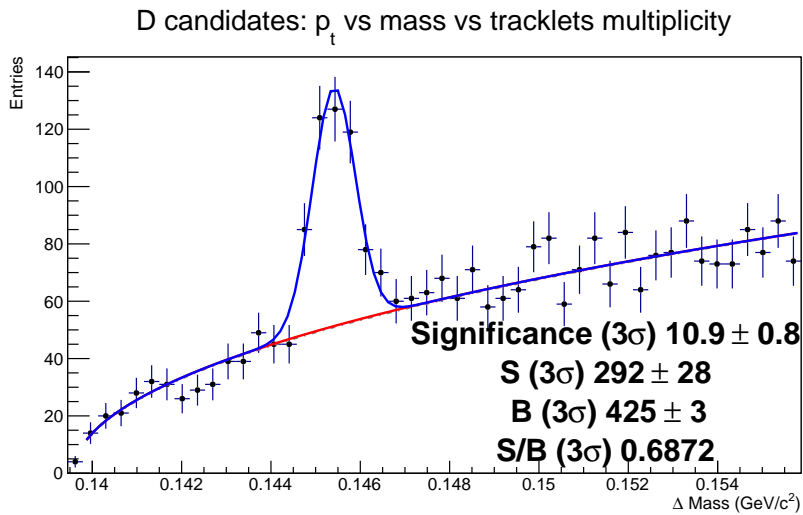
Figure 4.3: ΔM distribution of multiplicity [14-19] and p_T [1-2] GeV/ c .

candidates is optimized by removing the ones where the fit over the data in the ΔM distribution has a significance is much lower than 3σ . If the significance is just below 3σ then we need to consult the fit, if the fit of the peak is in good agreement with the data in the peak interval than it will not be cut. Figure 4.3 shows an example where the significance is below 3σ but it still contain a distinguishable peak from the background.

It is also possible to rebin the ΔM distribution histogram. What it does is basically summing up neighboring bins resulting into a new bin. Its new value will be the summed value of the old bins and positioned at the average position of the neighboring bins. Figure 4.5 is an example of the method, it shows how this method can help to get a more clear peak with respect to the background. Figure 4.6 shows a summary of the ΔM distribution of five p_T intervals at multiplicity [31-49]. In the distribution of p_T [1-2] GeV/ c the peak in the gaussian fitting region is barely distinguishable from the background, thus resulting in a low significance ($\mathcal{S}(3\sigma) = 2.0 \pm 1.1$). This then will not be considered in the further analysis.



(a)



(b)

Figure 4.4: Two ΔM distributions, both at multiplicity [31-49] and p_T [4-8] GeV/c . (a) is without PID and (b) is with PID using TOF and TPC with a cut of 3σ .

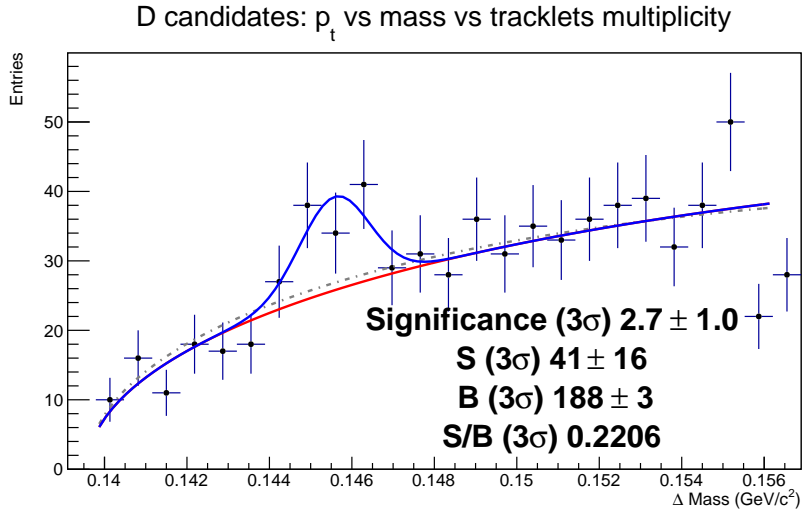
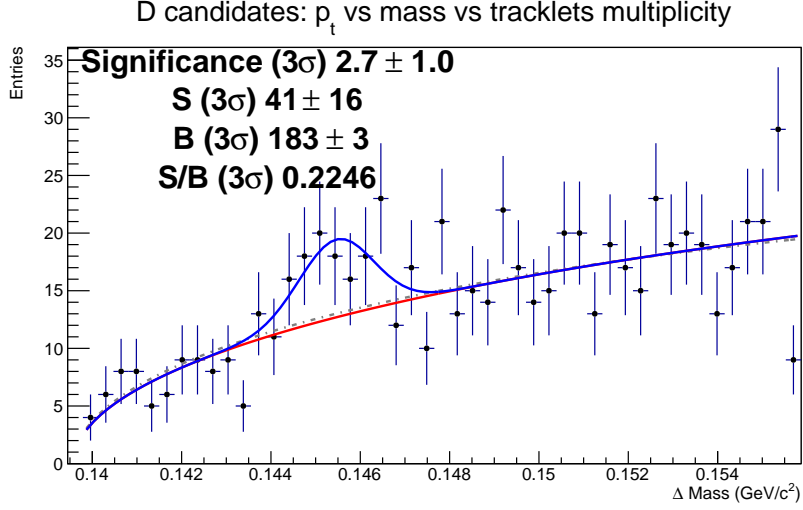
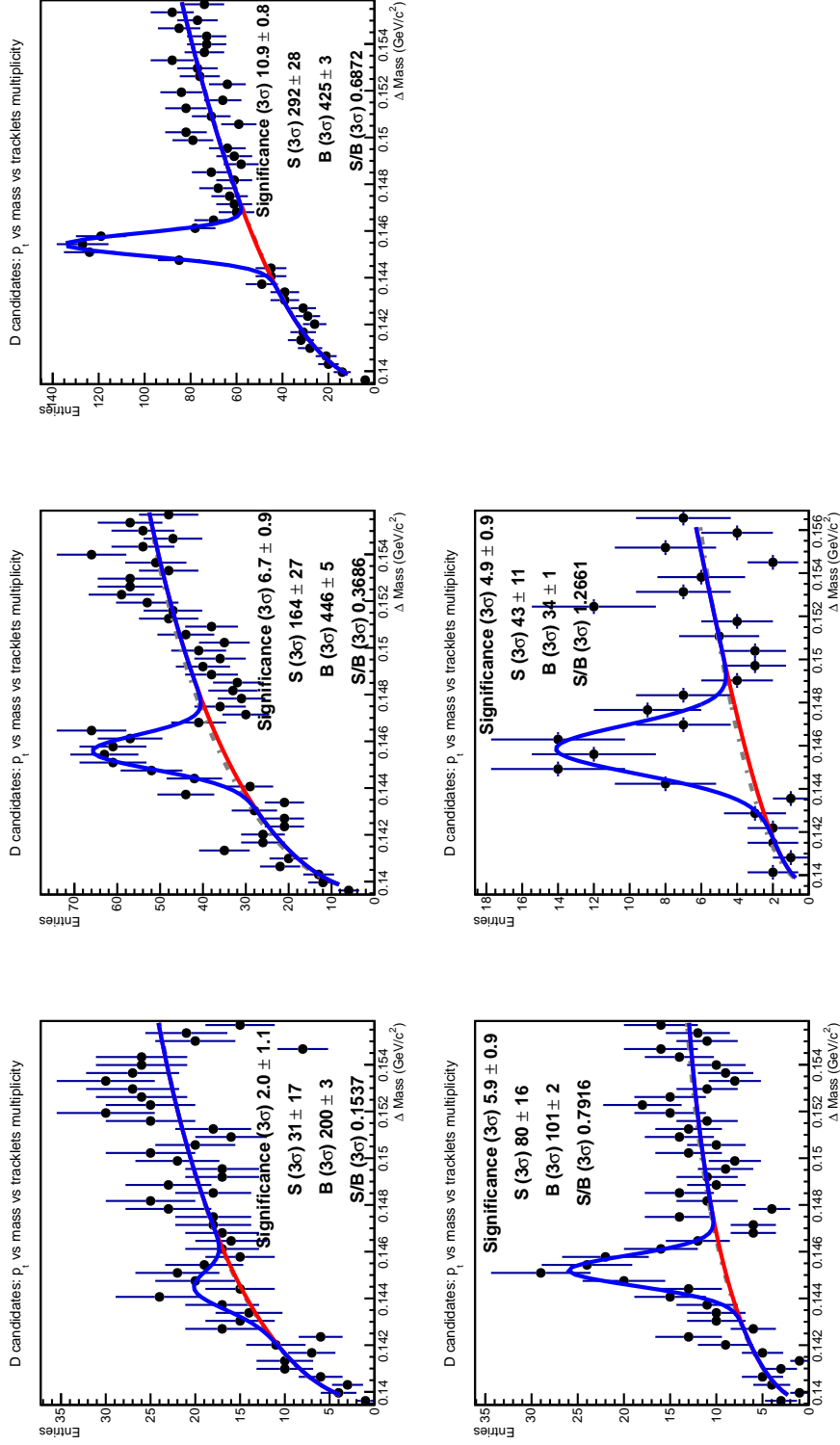


Figure 4.5: ΔM distribution of multiplicity [20-30] and p_T [1-2] GeV/ c . (a) is the original non rebinned version and (b) is when it is rebinned by summing two neighboring bins.

Figure 4.6: ΔM distribution of the multiplicity bin [31-49] for the p_T intervals: [1-2], [2-4], [4-8], [8-12] and [12-24] GeV/c.

Chapter 5

Yield extraction

To extract the D^{*+} yield from the ΔM distribution mentioned earlier, we first need to fit a function to the data points. This function is a sum of the background function and a gaussian given by equation 5.1.

$$\begin{aligned} f_{bkg}(x) &= a\sqrt{x - m_\pi}e^{b(x - m_\pi)}, \\ f_{peak}(x) &= \frac{A}{\sqrt{2\pi\sigma^2}}e^{-\frac{(x-d)^2}{2\sigma^2}}, \\ f_{fit}(x) &= f_{bkg} + f_{peak}. \end{aligned} \tag{5.1}$$

Here a , b , d , σ , and A are all fitting parameters, where σ is also the gaussian width. For a possible candidate, we should expect a peak near 145.421 ± 0.010 MeV/ c^2 to arise. Then by taking the integral of the gaussian in the signal region (3σ width), the yield is obtained. Table 5.1 shows the yields of different p_T intervals (minimum of 1 GeV/ c to a maximum of 24 GeV/ c), different multiplicity intervals (minimum of 1 to a maximum of 100) and of the minimum bias (multiplicity interval [1-100]). The last multiplicity interval [50-100], are from a data set where a high multiplicity trigger was used.

The empty spaces are the ΔM distributions where it was either not possible to fit a gaussian around 145.421 ± 0.010 MeV/ c^2 , or the significance was far below 3σ .

Table 5.1 shows that the yields with the smallest uncertainty margins are in the p_T interval [4-8] GeV/ c and the yields with the highest uncertainty margins are at the lowest and highest p_T intervals. In the introduction it was mentioned that at medium p_T interval we would expect the narrowest peak. We then would expect that for the gaussian width, σ would show a minimum at p_T [4-8]. In figure 5.1 the sigma is plotted against p_T for each multiplicity interval and it shows that overall the minimum is at p_T [2-4] and [4-8] GeV/ c . Section A.1 will discuss in more detail the sigmas at p_T [1-2] GeV/ c and the two points at p_T [12-24] that have a very low value with respect of the other three.

p_T GeV/c	Raw Yield mult[1-8]	p_T GeV/c	Raw Yield mult[9-13]
1-2		1-2	
2-4	46 \pm 8	2-4	80 \pm 13
4-8	84 \pm 11	4-8	199 \pm 19
8-12	19 \pm 6 (No PID)	8-12	52 \pm 11
12-24		12-24	

p_T GeV/c	Raw Yield mult[14-19]	p_T GeV/c	Raw Yield mult[20-30]
1-2	20 \pm 8	1-2	
2-4	155 \pm 19	2-4	207 \pm 25
4-8	255 \pm 22	4-8	414 \pm 32
8-12	84 \pm 12	8-12	140 \pm 18
12-24	24 \pm 6	12-24	53 \pm 12

p_T GeV/c	Raw Yield mult[31-49]	p_T GeV/c	Raw Yield mult[50-100]
1-2		1-2	
2-4	164 \pm 27	2-4	58 \pm 18
4-8	293 \pm 28	4-8	124 \pm 29
8-12	80 \pm 16	8-12	
12-24	44 \pm 11	12-24	18 \pm 7

p_T GeV/c	Raw Yield mult[1-100]
1-2	92 \pm 27
2-4	674 \pm 46
4-8	1260 \pm 55
8-12	393 \pm 29
12-24	137 \pm 19

Table 5.1: The extracted yield and minimum bias yield with a PID cut of 3σ TPC and TOF.

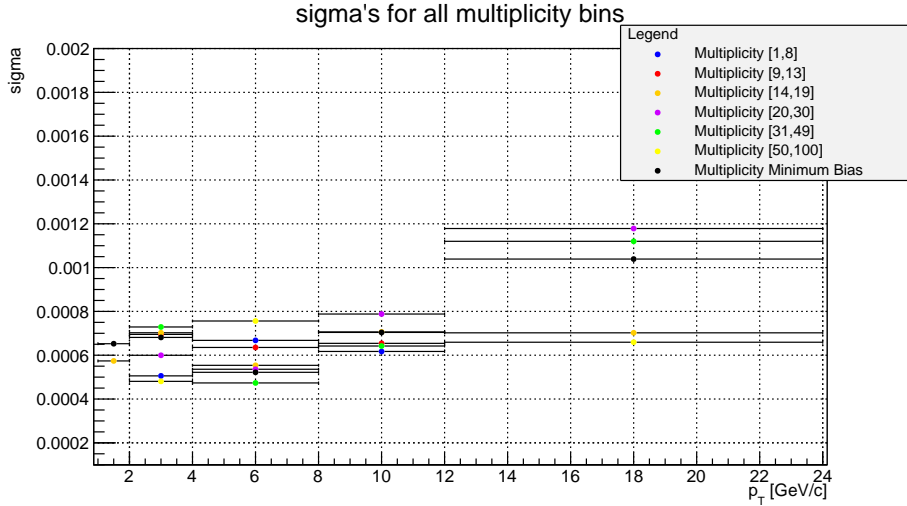


Figure 5.1: Here the values of σ are the width of the fitted gaussian in the ΔM distribution versus p_T for various multiplicity intervals.

Chapter 6

Systematics

For the study of the systematic uncertainty of the extracted standard yield, it is important to know how stable the yield is when we change the parameters, fit functions, fit intervals, etc. To get an idea of the systematic uncertainty, the parameter, interval or fit function is changed and then the yield is extracted (see section 6.1). Then by taking the ratio of this new yield with respect to the standard yield, we get the spread which tells us the stability of the yield under the change of parameters. This way we will obtain an estimation of the systematical uncertainty. For the systematics two values are extracted, the maximum spread and the root mean square (RMS) of the ratio spread in each p_T and multiplicity interval. The maximum spread would give us a safe estimation of the systematics, but risk the possibility of having to high uncertainties. Thus our results will risk losing its physical meaning. To retain its physical meaning without getting to low on the systematics we use the RMS, defined as:

$$\sigma_{\text{RMS}} = \sqrt{\frac{\sum_{i=1}^N \sigma_i^2}{N}}, \quad (6.1)$$

σ_{RMS} is the RMS, σ_i is one of the ratio spreads in the p_T and multiplicity interval with N number of ratios. N is 5 if no ratios are excluded (see appendix A.2).

6.1 Systematics on the yield extraction

The yield extracted from the standard fitted ΔM distribution has a mass range of [0.1398-0.156] GeV/ c^2 , the fit function is mentioned in chapter 5. Then the following changes are made:

- Changes in the mass range of the fitted ΔM distribution.
- Change in the background function to $f_{bkg2} = a(x - m_\pi)^b$.
- Bin counting with respect to the background function in the mass range [0.1398-0.156] GeV/ c^2 .
- Bin counting with respect to the background function in the mass range [0.1398-0.160] GeV/ c^2 .

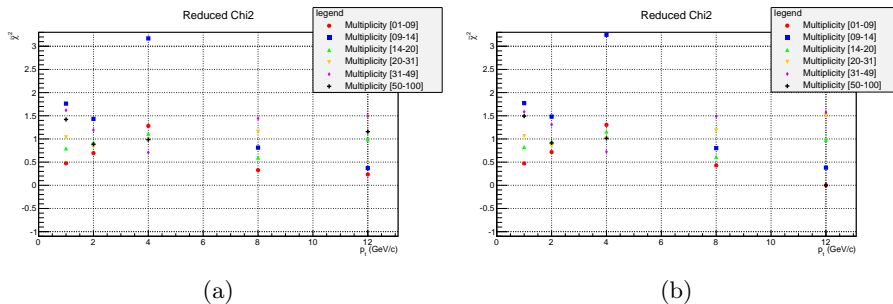


Figure 6.1: (a) Is χ^2/ndf of f_{bkg2} (ndf is the number of degrees of freedom). (b) is χ^2/ndf of f_{bkg} .

From each of these changes we extract the yield again. The reason for doing this will be explained in section 6.2.

6.1.1 Different invariant mass ranges

The reason why the mass range of the ΔM distribution is expanded is that we want to include more background, so that we can analyze the change in the yield. The mass range is varied from $[0.1398-0.156]$ to $[0.1398-0.160]$ and $[0.1398-0.165]$ GeV/c^2 . If the background would show significant peaks at higher masses, caused by background fluctuation, then this would influence the gaussian significantly. Giving a gaussian that differs significantly from the standard one. The integral of this gaussian will be extracted in the same way the standard yield is extracted.

6.1.2 Different background function

By changing the background function:

$$a\sqrt{x - m_\pi}e^{-b(x - m_\pi)} \implies a(x - m_\pi)^b, \quad (6.2)$$

one can look at how the gaussian may change when using a different fit function over the background. Figure 6.1 shows the χ^2/ndf of the two different background functions. It shows that χ^2/ndf of the two fits are almost alike. The integral of the gaussian will be extracted here.

6.1.3 Bin counting

The final method is called bin counting. This method will sum up each bin within the width of 3σ of the peak and subtract the fitted background in that region. This can be illustrated by the formula:

$$\sum_{i \in \{p-3\sigma, p+3\sigma\}} (N_i - f_{bkg}(x_i)). \quad (6.3)$$

Here p is the position of the peak, σ is the gaussian width, N_i the number of entries in bin i and x_i the centre of bin i . In our case we have two different backgrounds to consider, one is just the fitted background f_{bkg} leaving the data

Mult. bin	interval
0	1-8
1	9-13
2	14-19
3	20-30
4	31-49
5	50-100

Table 6.1: Multiplicity intervals are defined in figure 6.2 to 6.7 in bin from 0 to 5.

in the region (3σ width) of the gaussian out. The other is the fitted background over all the data including those in the gaussian region, which would result into a higher background function, especially in the peak region. In our study on the systematics of the extracted yield we only look at the influence of the combinatorial background of the fit. Thus we only use the fitted background function leaving out the the data points in the gaussian region.

6.2 Results

Figures 6.2 to 6.7 show the ratio of the extracted yields discussed in section 6.1 with respect to the standard yield,

$$\mathcal{R} = \frac{\text{yield from changed variables}}{\text{yield from standard variables}}. \quad (6.4)$$

Table 6.2 contains the systematic uncertainty (RMS) and the maximum spread extracted from the ratios plotted in the figures 6.2 to 6.7.

For the convenience of the figures 6.2 to 6.7, the iplicity interval has been renamed (see table 6.1). The overall maximum spread of the different ratios are minimized at the middle for example p_T [4-8] GeV/ c (see figure 6.4). It seems that the spread grows at higher or lower p_T , this also seems the case for multiplicity. This means that the gaussian fit for in the ΔM distribution at p_T [4-8] GeV/ c is more stable with respect to changes in the variables than at higher or lower p_T . This results in a small systematical uncertainty in the middle p_T and multiplicity intervals. The stability of the gaussian will only decrease at higher or lower p_T and multiplicity, giving higher systematical uncertainties. This corresponds with figure 5.1 where the smallest gaussian widths are also at p_T [4-8] GeV/ c . Certain ratios at certain p_T and multiplicity intervals show a spread of $> 10\%$ or are significantly separated from the other ratios. These ratios will be discussed in detail in appendix A.2, some may be excluded in the systematical estimation. In table 6.2 the some ratios discussed in appendix A.2 will be excluded from the systematic uncertainty estimation.

Multiplicity	$p_T[1-2] \frac{\text{GeV}}{c}$	$p_T[2-4] \frac{\text{GeV}}{c}$	$p_T[4-8] \frac{\text{GeV}}{c}$	$p_T[8-12] \frac{\text{GeV}}{c}$	$p_T[12-24] \frac{\text{GeV}}{c}$
[1-8]		1% (2%)	3% (5%)	5% (9%)	
[9-13]		6% (8%)	5% (8%)	3% (4%)	
[14-19]	7% (12%)	1% (2%)	4% (6%)	2% (3%)	4% (4%)
[20-30]		2% (4%)	5% (7%)	2% (3%)	3% (5%)
[31-49]		6% (10%)	1% (2%)	5% (9%)	4% (5%)
[50-100]		5% (11%)	5% (9%)		8% (11%)
[01-100]	4% (6%)	2% (3%)	3% (5%)	1% (2%)	3% (4%)

Table 6.2: The systematic uncertainties for different multiplicity and p_T intervals. The value between the brackets is the maximum spread. The ratio points discussed in appendix A.2 are ignored.

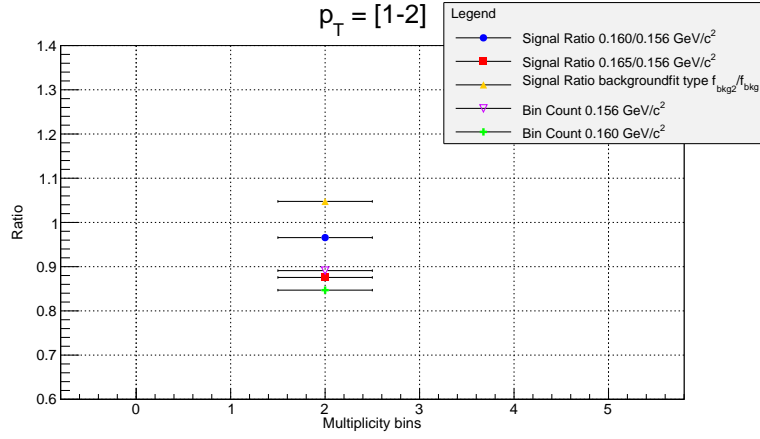


Figure 6.2: Ratios for p_T interval [1-2] GeV/c. Multiplicity bins are defined in table 6.1. Gaussian means the bins within the gaussian region of 3σ .

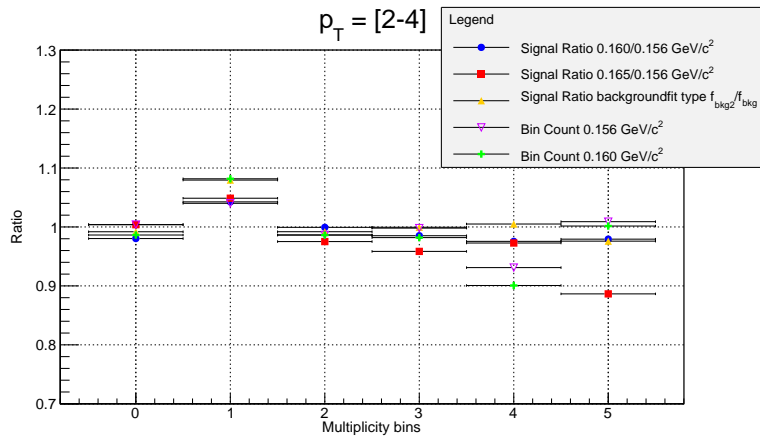


Figure 6.3: Ratios for p_T interval [2-4] GeV/c. Multiplicity bins are defined in table 6.1 Gaussian means the bins within the gaussian region of 3σ .

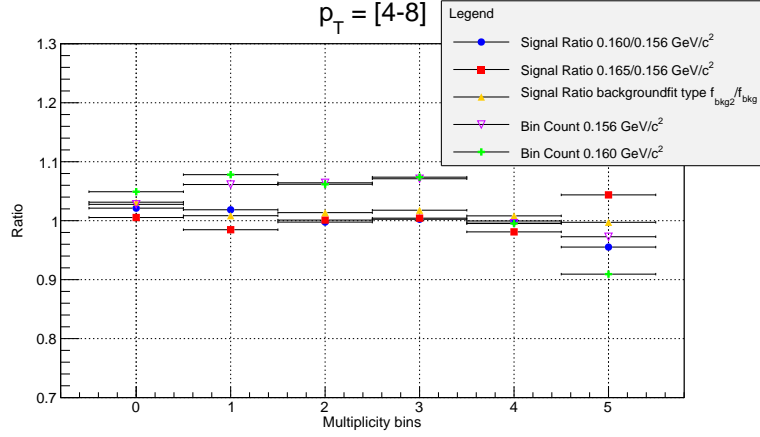


Figure 6.4: Ratios for p_T interval [4-8] GeV/c. Multiplicity bins are defined in table 6.1 Gaussian means the bins within the gaussian region of 3σ .

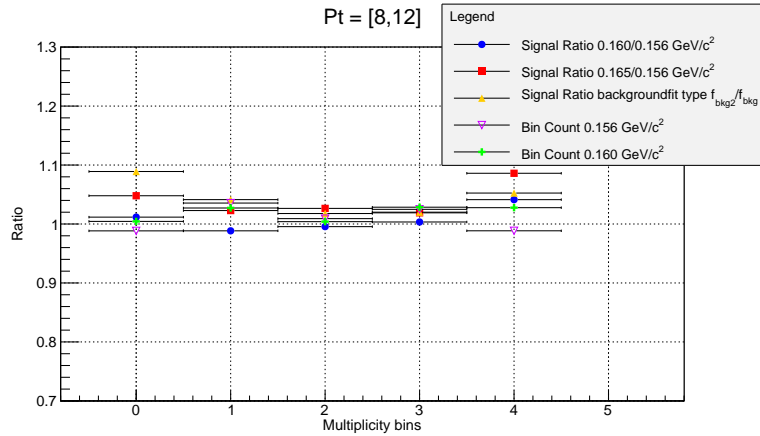


Figure 6.5: Ratios for p_T interval [8-12] GeV/c. Multiplicity bins are defined in table 6.1 Gaussian means the bins within the gaussian region of 3σ .

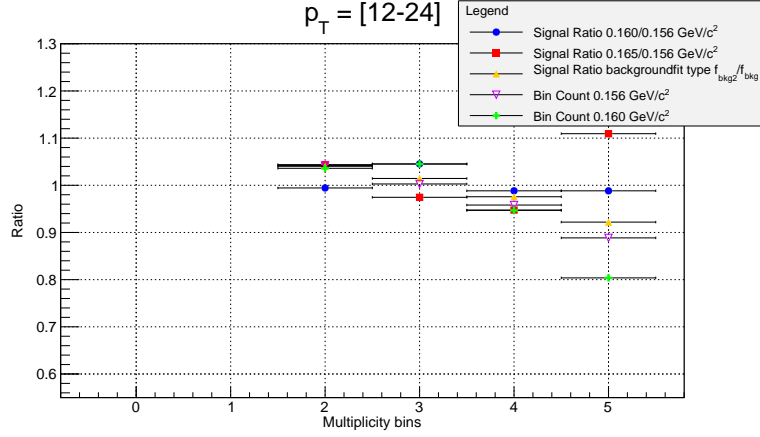


Figure 6.6: Ratios for p_T interval [12-24] GeV/c. Multiplicity bins are defined in table 6.1 Gaussian means the bins within the gaussian region of 3σ .

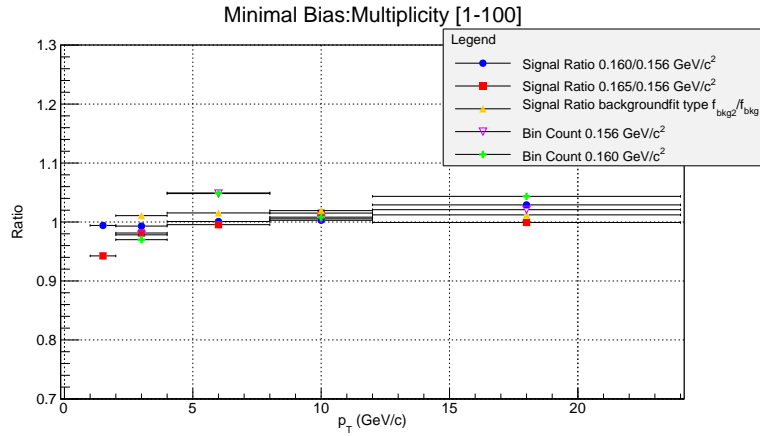


Figure 6.7: Ratios for the minimum bias. Multiplicity bins are defined in table 6.1 Gaussian means the bins within the gaussian region of 3σ .

Chapter 7

Efficiency corrections

Corrections are done using computer simulations of the pp collisions (see section 7.1). It keeps track of various variables for different steps. The most important steps used in this thesis are:

- Generated D^{*+} mesons with the acceptance of the detector.
- Final reconstructed D^{*+} mesons that pass the topological cuts and the PID cuts.

The variable saved for these steps is the D^{*+} p_T . The D^{*+} mesons in these steps are all created with a charm quark originating either directly (c-prompt) from the collision point or indirectly through beauty decay (b feed-down) in pp collisions.

7.1 Monte Carlo simulations

The Monte Carlo simulation, the name is borrowed from the casino's in Monte Carlo, is a method to simulate particle collisions. It is a computational algorithm that relies on repeated random sampling to obtain the probability distribution of the set of simulations, hence the name Monte Carlo simulations. The simulated events in this thesis are generated by the event generator PYTHIA. Based on pQCD it generates various high energy particle events such as:

- Soft and hard interactions.
- Parton showers.
- Multiple interactions.
- Fragmentation and decays.

The detector response is simulated by GEANT (GEometry ANd Tracking). These two simulators will provide us the simulation data on the reconstructed tracks and the generated tracks.

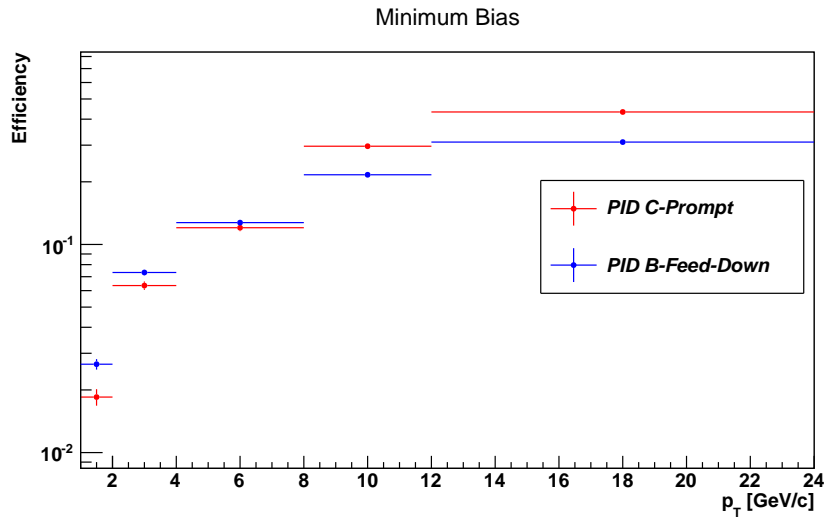


Figure 7.1: The efficiency of c-prompt and b feed-down with topological and PID selection cuts. Y axis is at logarithmic scale.

7.2 Efficiency

The efficiency is calculated from two data sets, lhc12a12 and lhc12a12bis. The generated p_T distribution of the D^{*+} within the detectors acceptance from the two data sets are summed. Also the generated p_T distribution of the final reconstructed D^{*+} that pass the topological cuts and PID cuts from the two data sets are summed.

There are two ways a charm quark can be produced in a pp collision, they are called c-prompt and b feed-down. The c-prompt is formed directly after a parton-parton collision. The charm in the b feed-down is a product from the decay a beauty quark $b \rightarrow c + W^-$. Figure 7.1 shows the efficiency of the c-prompt and b feed-down for the minimum bias with the topological and PID (3σ) selection cuts and its y axis in logarithmic scale.

This thesis focusses on how much multi-parton interactions may influence the charm production. This is why we are only interested in the charm quarks created directly from the collision (c-prompt). Because beauty quarks also have the probability to decay into charm quarks means that the data samples will contain a fraction that is contaminated with b feed-down charm quarks. Having the efficiency of the b feed-down is therefore useful to determine the size of this fraction. Figure 7.2 and 7.3 shows the efficiency of the charm production of both c-prompt and b feed-down for different multiplicity intervals with the topological and PID (3σ) selection cuts and its y axis in logarithmic scale.

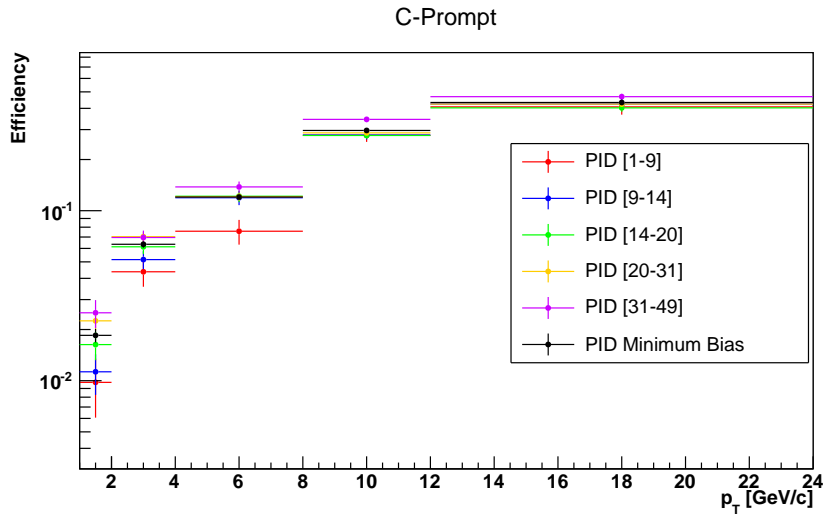


Figure 7.2: The efficiency of c-prompt with topological and PID selection cuts. Y axis is at logarithmic scale.

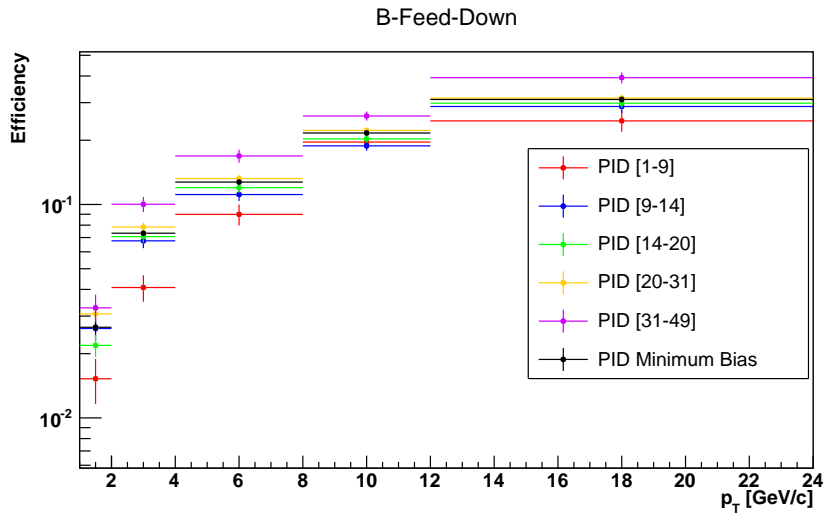


Figure 7.3: The efficiency of b feed-down with topological and PID selection cuts. Y axis is at logarithmic scale.

Chapter 8

Conclusions

The yield is extracted by integrating (over a width of 3σ) the gaussian fitted over the data points (see table 5.1). Table 5 shows that the fits at p_T [1-2] are excluded in this thesis for almost all multiplicity intervals due to the fit optimization. The systematics on the extracted yield is calculated from the spread of different ratios where the standard yield is divided by the extracted yield with a change in its variables mentioned in section 6.1 (see table 6.2). The data sets used are measured in the periods b, c, d and e in 2010 with a high multiplicity extra trigger sample measured in period e. The efficiency was calculated from two Monte Carlo data sets. Tables 8.1 and 8.2 shows the efficiency of c-prompt and b feed-down.

The number of events from the data samples used in this thesis is not the complete amount of event, but a fraction of the total amount of events. Because of this the thesis do not contain the full statistics of the measurements which is why some fits in the ΔM distribution give $< 3\sigma$ significance, for example the p_T [1-2] GeV/c fits. Having the full statistics could amplify the signal en constrain the background more, the significance thus scales with the number of events as: $\mathcal{S} \propto \sqrt{n}$. Thus we could get a better estimation on the systematic uncertainty for p_T [1-2] GeV/c.

8.1 Further research

In this thesis the raw yield is extracted from a fraction of the total amount of events from the measurements in the four periods. Thus the systematic uncertainty from different ΔM ranges, different background functions and the bin count (see sections 6.1.1, 6.1.2 and 6.1.3) are also from a fraction of the total amount of events. For using the total amount, it is expected that for p_T [1-2] GeV/c the signal peak will be much clearer with respect to the background and the significance will rise significantly.

The efficiency is done for the c-prompt and b feed-down charm production for multiplicity up to 49. Although the efficiency have low uncertainties up to the multiplicity of 49, the uncertainty will increase at higher multiplicity up to 40 %, so the efficiency is now only certain for low multiplicity. There are still certain cases that have to be done:

- This thesis has left out the systematics of the PID selection cut. For a

better estimation on the systematics, one could include the systematics of the PID selection cuts.

- The systematics and yield in this thesis are from data samples with partial statistics, the same must be done with the full statistics (the total amount of events measured in the four periods) to get a better and more accurate reading of the systematics and yield.
- More simulations are needed with more generated events to get better statistics for the efficiency at high multiplicity.
- We need the relative yield at different multiplicity with the full statistics and systematics.
- The results of the relative yield must be compared with theoretical predictions from single parton models. To conclude if multi-parton interactions play a major role in pp collisions.

If there we find clear proof that multi-parton interactions play an increasingly larger role in high energy pp collisions, then it could lead to new future research possibilities:

- Further research may be on the analysis of multi-parton interactions in Pb-Pb and/or p-Pb collisions.
- Currently the LHC is planned to undergo an upgrade to double the energy to $\sqrt{s} = 14$ TeV. A possible study can be on how much the influence of multi-parton interaction would increase at higher collision energy.

Multiplicity	p_T [1-2] $\frac{\text{GeV}}{c}$	p_T [2-4] $\frac{\text{GeV}}{c}$	p_T [4-8] $\frac{\text{GeV}}{c}$	p_T [8-12] $\frac{\text{GeV}}{c}$	p_T [12-24] $\frac{\text{GeV}}{c}$
[1-8]		4.4 \pm 0.8 %	7.6 \pm 1.3 %	27.8 \pm 2.4 %	
[9-13]		5.2 \pm 0.6 %	11.9 \pm 1.1 %	27.9 \pm 1.6 %	
[14-19]	1.6 \pm 0.3 %	6.1 \pm 0.6 %	12.2 \pm 0.9 %	27.7 \pm 1.3 %	40.3 \pm 2.1 %
[20-30]		7.0 \pm 0.5 %	12.1 \pm 0.7 %	28.7 \pm 0.9 %	42.3 \pm 1.4 %
[31-49]		7.0 \pm 0.7 %	13.8 \pm 1.0 %		46.9 \pm 2.0 %
[01-100]	1.8 \pm 0.2 %	6.3 \pm 0.3 %	12.0 \pm 0.4 %	29.7 \pm 0.6 %	43.3 \pm 1.0 %

Table 8.1: The efficiency of c-prompt calculated in this thesis.

Multiplicity	p_T [1-2] $\frac{\text{GeV}}{c}$	p_T [2-4] $\frac{\text{GeV}}{c}$	p_T [4-8] $\frac{\text{GeV}}{c}$	p_T [8-12] $\frac{\text{GeV}}{c}$	p_T [12-24] $\frac{\text{GeV}}{c}$
[1-8]		4.1 \pm 0.6 %	9.0 \pm 1.0 %	19.6 \pm 1.5 %	
[9-13]		6.8 \pm 0.5 %	11.1 \pm 0.7 %	18.8 \pm 1.0 %	
[14-19]	2.2 \pm 0.3 %	7.1 \pm 0.4 %	12.0 \pm 0.6 %	20.3 \pm 0.8 %	29.8 \pm 1.5 %
[20-30]		7.8 \pm 0.4 %	13.2 \pm 0.6 %	22.2 \pm 0.7 %	31.5 \pm 1.2 %
[31-49]		10.0 \pm 0.8 %	16.9 \pm 1.2 %		39.3 \pm 2.3 %
[01-100]	2.7 \pm 0.2 %	7.3 \pm 0.2 %	12.7 \pm 0.4 %	21.6 \pm 0.4 %	31.0 \pm 0.8 %

Table 8.2: The efficiency of b feed-down calculated in this thesis.

Appendix A

Discussions

A.1 Sigmas

Figure 5.1 shows the sigmas plotted versus p_T . We should expect that the overall value of the sigmas would be at a minimum at roughly p_T [2-4] and [4-8] GeV/ c and increase at higher and lower p_T . But the overall value at p_T [1-2] GeV/ c does not increase and there are two sigma values at p_T [12-24] GeV/ c that shows significantly lower values with respect to the other sigma value point at that p_T interval.

The problem at p_T [1-2] is that due to the partial statistics used, we cannot fit a gaussian over the data point in the ΔM distribution. Thus we cannot judge the overall value based on only one multiplicity interval and the minimum bias. For p_T [12-24] and multiplicity [14-19] and [50-100] we need to look more closely to the ΔM distribution, figures A.1a and A.1b shows these ΔM distribution. Both figures shows that the peak consist of just three to four data points, resulting in a relatively narrow peak. It also shows the consequence of using partial statistics, figure A.1a shows barely any background while figure A.1b shows strong background fluctuations. If having the full statistics, one should expect less background fluctuations and the width of the peak would increase.

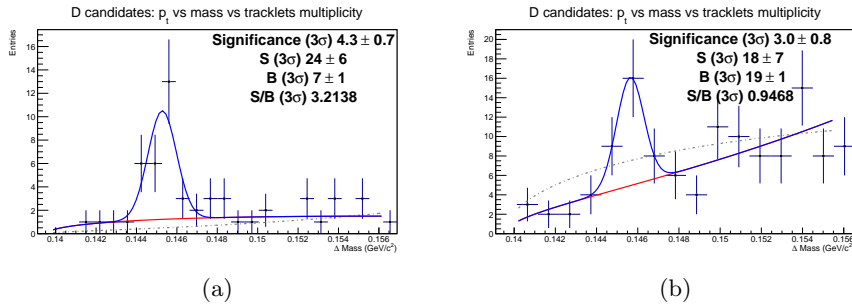


Figure A.1: (a) is the ΔM distribution at p_T [12-24] and multiplicity [14-19] and (b) at p_T [12-24] and multiplicity [50-100].

A.2 Ratios

Some ratio point shown in the figures of section 6 are either significantly off ($> 10\%$). This will try to explain why the spread of the ratio point are so large and argue if the ratio can be ignored in the calculation of the systematic uncertainty. If certain ratios are excluded from the systematic estimation, then they will not be included in the RMS and will lose the possibility to be labeled as the maximum spread. The ratios that will be discussed here are:

1. The bin counts of $0.156 \text{ GeV}/c^2$ at p_T [1-2] GeV/c and multiplicity [14-19].
2. The bin counts of $0.160 \text{ GeV}/c^2$ at p_T [1-2] GeV/c and multiplicity [14-19].
3. The signal ratio of mass ranges [0.1398-0.156] and [0.1398-0.165] GeV/c^2 at p_T [1-2] GeV/c and multiplicity [14-19].
4. The signal ratio of mass ranges [0.1398-0.156] and [0.1398-0.165] GeV/c^2 at p_T [2-4] GeV/c and multiplicity [50-100].
5. The bin counts of $0.156 \text{ GeV}/c^2$ at p_T [12-24] GeV/c and multiplicity [50-100].
6. The bin counts of $0.160 \text{ GeV}/c^2$ at p_T [12-24] GeV/c and multiplicity [50-100].
7. The signal ratio of mass ranges [0.1398-0.156] and [0.1398-0.165] GeV/c^2 at p_T [12-24] GeV/c and multiplicity [50-100].

For the cases (1), (2) and (3), we will consult figure A.2. There it shows strong background fluctuations, the data points show a significant drop just before the gaussian peak. At figure A.2b we can see that the background keeps fluctuating giving another peak at around 0.152 and another at $0.161 \text{ GeV}/c^2$ and after each peak a steep drop to below the fit function. This causes instability on the yield and bin counting when varying the mass range. Figure A.2 shows that when we expand the mass range to [0.1398-0.165] GeV/c^2 a new peak will show up at $0.161 \text{ GeV}/c^2$ which will significantly influence the yield, thus we will only exclude the ratio of case (3). Please note that although the ratios of the cases (1) and (2) will be included in the systematics estimation, thus giving a greater systematics uncertainty, that there is a non-neglectable possibility that the peak fitted with the gaussian is mainly due to background fluctuations. The full statistical analysis is therefore needed.

Figure A.3 shows the ΔM distribution for case (4). It shows no strong fluctuations of the background. Although the background starts show a steeper increase at roughly 0.152 to $0.156 \text{ GeV}/c^2$ with few small fluctuations afterwards, the significance is still above 3σ . Thus we will not exclude this ratio in the systematic estimation.

Figure A.4 shows the ΔM distributions of cases (5), (6) and (7). Figure A.4b shows that at larger mass ranges the gaussian fit becomes unrealistic which explains the instability of the yield. Also this unrealistic narrow gaussian would explain the large spread of the bin count ratio at the mass range [0.1398-0.160] GeV/c^2 , our bin counting is done within the region of 3σ and a narrow gaussian correspond to a small σ . Therefore the value of the bin count is much smaller than the standard yield. Due to the unrealistic gaussian fitted over the data

point we will exclude the ratios of the cases (6) and (7). Figure A.4a shows a more realistic fitted gaussian, thus we will not exclude the ratio of case (5) in the systematic estimation.

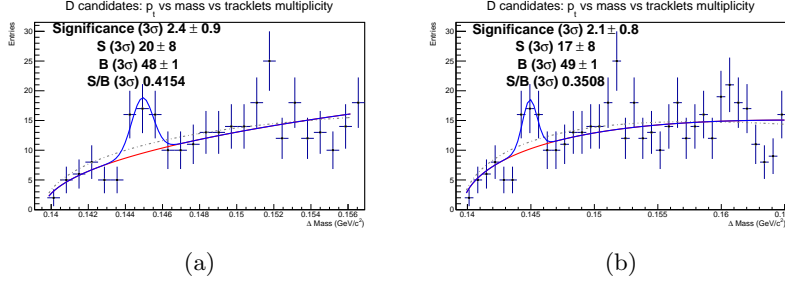


Figure A.2: The ΔM distribution at p_T [1-2] GeV/c and multiplicity [14-19] plotted in the mass range (a) \rightarrow [0.1398-0.156] GeV/c² and (b) \rightarrow [0.1398-0.165] GeV/c².

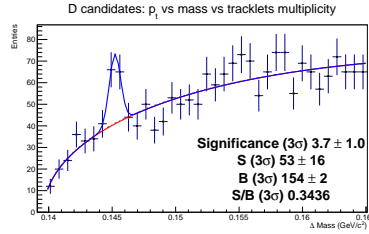


Figure A.3: The ΔM distribution at p_T [2-4] and multiplicity [50-100].

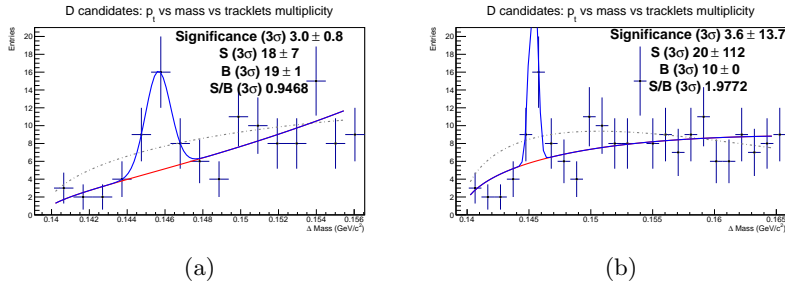


Figure A.4: The ΔM distribution at p_T [12-24] GeV/c and multiplicity [50-100] plotted in the mass range (a) \rightarrow [0.1398-0.156] GeV/c² and (b) \rightarrow [0.1398-0.165] GeV/c².

Acknowledgements

I want to thank my head supervisor Dr. André Mischke for giving me a place in his research group and guidance during my research. And I also want to thank my daily supervisor Dr. Alessandro Grelli for taking so much of his time to help and guide me through my research each day. I want to thank all the people of the subatomic physics group which is too large for me to thank (and remember the name) individually for being so open and helpful. And the great group of bachelor students livening up the student room and being there for each other when one needed help. I also want to thank Dr. Marco van Leeuwen and Dr. Gerhard Blab for helping me with my presentation theme. And I must to thank my parents for their loving care and not yelling at me for neglecting them these past few months.

I like to acknowledge the authors of the thesis's and papers I have used as reference for my own thesis.

And finally I want to thank the reader for taking some of his/her time to look through my thesis.

Bibliography

- [1] S. Bethke, *The 2009 World Average of α_s* , Eur. Phys. J., **C64**, 2009. arXiv:hep-ph/0908.1135.
- [2] S. Baumgart, *A Study of Open Charm Production in Heavy Ion Collisions of Center-of-Mass Energy 200 GeV per Nucleon*, Ph.D. thesis, Yale University, 2009.
- [3] T. Sjostrand and P.Z. Skands, *Multiple Interactions and the Structure of Beam Remnants*. JHEP, **0403** p. 053, 2004. arXiv:hep-ph/0402078.
- [4] E. Sicking, *Multiplicity Dependence of Two-Particle Angular Correlations in Proton-Proton Collisions Measured with ALICE at the LHC*, Ph. D. thesis, Münster University, 2012.
- [5] T. Sjöstrand and M. van Zijl, *Multiple Parton-Parton Interactions in an Impact Parameter Picture*, Phys. Lett., **B188** pp 149-154, 1987.
- [6] E. Sicking, *Multiple Parton Interaction in ALICE*, Presentation CERN LHC Seminar, 2013.
- [7] J. Beringer et al. (Particle Data Group), Phys. Rev. **D86**, 010001, 2012.
- [8] The ALICE Collaboration, *Physics Performance Report Vol.1*, J. Phys. G: Nucl. Part. Phys. 30 1517-1763, 2004.
- [9] <http://wa98.web.cern.ch/WA98/sdd.shtml>, Last modified by H. Schlagheck (2000).
- [10] <http://aliceinfo.cern.ch/TPC/node/7>, ALICE@CERN 2010.
- [11] L. Bryngemark *Charged pion identification at high pT in ALICE using TPC dE/dx .*, 201. arXiv:1109.1896 [hep-ex].
- [12] C. Lippmann *Particle identification in ALICE: an extra boost in QGP studies.*, 2012. http://alicematters.web.cern.ch/?q=CL_PID2.
- [13] J. van der Maarel, *D^{*+} analysis in proton-proton collisions at $\sqrt{s} = 7$ TeV at ALICE*, Bachelor thesis, Utrecht University, 2011.
- [14] C. Ivan, *Open Charm Analysis with the ALICE detector in p-p collisions at LHC*, Ph.D. thesis, Utrecht University, 2009.